

FINAL REPORT

Part I

ETO Cloud Studies for FIRE II

NASA Grant No. NAG-1-868

1 June 1990 - 31 May 1992

LANGLEY
GRANT
IN-47-CR
104859
P-39

Prepared by

Kenneth Sassen

Department of Meteorology
University of Utah
Salt Lake City, UT 84112

24 June 1992

(NASA-CR-190472) ETO CLOUD STUDIES FOR FIRE
2, PART 1 Final Report, 1 Jun. 1990 - 31 May
1992 (Utah Univ.) 30 p

N92-29087

Unclas
G3/47 0104859

ABSTRACT

ORIGINAL CONTAINS
COLOR ILLUSTRATIONS

This research program in support of Project FIRE involved two efforts. The results of the first effort, which were in direct support of the Extended Time Observations (ETO) component, are described here in Part-I. Over the period from June 1990 through May 1991, our remote sensing systems were applied to providing ground-truth cirrus cloud observations for a total of 71 NOAA polar orbiting satellite overpasses. (Chronological tables of this effort are provided.) The primary remote sensor was a dual-polarization ruby ($0.694\ \mu\text{m}$ wavelength) lidar, although mid-way through the program we added a number of radiometers to assess the surface radiation budget and cirrus cloud infrared emittance, and some supplemental observations from a K_a -band ($8.6\ \text{mm}$) radar were also collected. These studies were conducted from the Facility for Atmospheric Remote Sensing (FARS) at $40^\circ\ 46'\ 00''$ north latitude and $111^\circ\ 49'\ 38''$ east longitude. We also investigated the unusual characteristics of a subset of ETO case studies involving cirrus that generated solar and lunar corona displays. As we reported recently (reprint attached), these cirrus were atypically high and cold in relation to our total midlatitude cloud sample, and were comprised of unexpectedly small ice crystals from 10 to $30\ \mu\text{m}$ in dimension. This finding lends some credence to the so-called cirrus small particle radiative anomaly, but only for very cold ($< -60^\circ\text{C}$) cirrus clouds. In a supplement to this report, we will describe the design and testing of a prototype cirrus cloud polar nephelometer, which we constructed as part of our second research effort, to allow scattering phase functions to be obtained in future in situ cirrus research.

I. Introduction

Our involvement in the First ISCCP Regional Experiment began with the deployment of the Mobile Polarization Lidar unit at Wausau, WI, during the October-November 1986 cirrus cloud Intensive Field Observations (IFO) campaign. Since that time we have nearly continuously collected remote sensing cirrus cloud measurements in support of the Extended Time Observations (ETO) effort from the University of Utah Facility for Atmospheric Remote Sensing (FARS). These measurements are collected in conjunction with local NOAA polar-orbiting satellite overpasses to provide much needed "ground-truth" data to help interpret the satellite imagery and test ISCCP cloud retrieval algorithms. In this report we summarize our observational and analyses efforts in support of the FIRE ETO program over the 1 June 1990 to 31 May 1991 period of performance for ETO support. Since our efforts in this regard are continuing into Phase II of Project FIRE, final data analysis and archival are awaiting the completion of our research.

II. Research Facilities

FARS is located on the edge of the University of Utah campus at an elevation of 1.52 km MSL at 40° 46' 00" N and 111° 49' 38" E. The kernel of instrumentation at FARS used in cirrus cloud research includes a dual-polarization ruby lidar system, which provides uncalibrated backscatter and linear depolarization (see Sassen 1991a) data, and a suite of roof-mounted visible and infrared radiometers. One of the passive instruments, a midinfrared narrowbeam radiometer, is coaligned with the lidar to obtain cirrus cloud infrared emittances using the LIRAD method described by Platt 1979, and Platt and Dilly 1981. The specifications of these instruments are provided in Table 1, although it should be

Table 1. Regular ETO Atmospheric Remote Sensing Research Capabilities at FARS.

1.	<u>Passive Remote Sensors</u>
a.	Net Flux Pyrrometers
b.	Narrow-beam (0.14°) 9.5-11.5 μ m radiometer (co-aligned with lidar)
c.	Precision Infrared Radiometer
d.	Pyranometer, 0.3-2.8 μ m broadband visible
e.	Rotating Shadowband Radiometer (0.63-2.5 μ m)
f.	Pyrheliometer (0.63-2.8 μ) with solar tracker
g.	All-sky 35mm photography (black-and-white, and color)
2.	<u>Dual Polarization Ruby Lidar</u>
	- Manually "tiltable" $\pm 5^\circ$ from zenith
	- 30 s PRF
	- 7.5 minimum range resolution
	- Maximum 2K per channel data record length
	- 1-3 mrad receiver beamwidths
	- 0.694 μ m wavelength, 1.5 J output
3.	<u>Meteorological Sensors</u>
a.	Temperature
b.	Relative Humidity

Table 2. Specifications of the K_a-band Radar System Deployed at FARS

Wavelength (cm)	0.86
Peak Power (W)	1.0×10^5
PRF (Hz)	937
Pulse Width (μ s)	0.5
Sample Width (m)	100
Number of Range Gates	512
Pulses Averaged	64-128
Beamwidth (°)	0.5
Radar System Gain (dB)	48.5
Antenna Diameter (m)	1.3

recognized that the passive remote sensors in items 1b-f were first incorporated into the FARS data acquisition scheme during February 1991. Moreover, a K_a -band microwave radar, whose specifications are given in Table 2, only supported our ETO effort from July 1990 to November 1991.

The ETO remote sensing data records are supplemented by case-by-case data files containing the twice-daily radiosonde profiles launched from the Salt lake City National Weather Service station (12 km to the west of our field site), as well as hard copies of products available from our advanced synoptic laboratory, including satellite imagery and upper air charts.

III. ETO Operations

Compiled in Appendix 1 are the ETO Data Summary sheets inclusive of the period of performance of concern here, and in Table A1, an explanation sheet for the various column entries. Note that the ETO-supporting listings are identified by asterisks in the Date column (i.e., for days 5-10 and 20-25 of each month). Other listings show cirrus cloud data collection on non-primary days, which were funded from other funding sources (the National Science Foundation and the Analytical Sciences Corporation), but which will be made available to FIRE researchers and included in our climatological cirrus research component. The observation sets are typically collected for 1-3h periods bracketing the local overpass to obtain data on cirrus cloud structural variability, encompass consecutive overpasses, and make allowances for inaccuracies in the predicted ephemeris.

A total of 71 of satellite overpasses were collected in accordance with the FIRE ETO timetables. Of this total, 9 datasets contained supporting K_a -band radar data, 25 were

appropriate for LIRAD study using the midinfrared radiometer, and 34 involved the full radiometer component listed in Table 1. This level of ETO support was somewhat less than had been anticipated due to unreliable ruby laser operation (and a major two-month long breakdown), as well as occasional lapses in the ETO overpass timetables (provided by NASA). The unreliable laser transmitter has since been replaced.

IV. ETO Case Study Analysis

We previously recognized the need to determine if our enlarging ETO dataset could be applied to researching the important question of the presence of very small undetected cirrus cloud particles (see Sassen et al. 1990), and identified a subset of our data sample that could be useful in this area. Recent radiative transfer simulations of cirrus clouds based on various observation sets (Platt et al. 1989; Minnis et al. 1990; Wielicki et al. 1990; Kinne et al. 1992) suggested that numerous small particles may be present in cirrus, or at least this condition would provide for more favorable comparison between simulations and measurements.

The ETO cirrus data subset that could shed light on this problem area involves studies of corona-producing cirrus, which, owing to fundamental scattering principles, must contain relatively small particles. Our analysis indicated that such occurrences in cirrus clouds were relatively rare in our sample, but that the ice crystals responsible were indeed quite small, ranging from about 10 to 30 μm in dimension. All occurrences were associated with unusually high and cold (-60° to -70°C) cirrus layers that straddled the tropopause. Thus, although it was demonstrated that some cirrus contained ice particles generally too small to be detected by current in situ probes, the conditions under which they occurred were much

too limited to provide justification for the so-called cirrus small particle radiative anomaly.

A reprint of the article (Sassen 1991b) is attached as Appendix 2.

V. References

- Kinne, S., T.P. Ackerman, A.J. Heymsfield, F.P.J. Valero, K. Sassen and J.D. Spinhirne, 1992: Cirrus microphysics and radiative transfer: Cloud field study on 28 October 1986. *Mon. Wea. Rev.*, **120**, 661-684.
- Minnis, P., D.F. Young, K. Sassen, J.M. Alvarez and C.J. Grund, 1990: The 27-28 October 1986 FIRE IFO cirrus case study: Cirrus parameter relationships derived from satellite and lidar data. *Mon. Wea. Rev.*, **118**, 2403-2425.
- Platt, C.M.R., 1979: Remote sensing of high clouds. I: Calculations of visible and infrared optical properties from lidar and radiometric measurements. *J. Appl. Meteor.*, **18**, 1130-1143.
- _____, and A.C. Dilley, 1981: Remote sensing of high clouds. IV: Observed temperature variations in cirrus optical properties. *J. Atmos. Sci.*, **38**, 1069-1082.
- _____, J.D. Spinhirne and W.D. Hart, 1989: Optical and microphysical properties of a cold cirrus cloud: Evidence for regions of small ice particles. *J. Geophys. Res.*, **94**, 11,151-11,164.
- Sassen, K., 1991a: The polarization lidar technique for cloud research: A review and current assessment. *Bull. Amer. Meteor. Soc.*, **72**, 1848-1866.
- _____, 1991b: Corona-producing cirrus cloud properties derived from polarization lidar and photographic analyses. *Appl Opt.*, **30**, 3421-3428.
- _____, A.J. Heymsfield and D.O'C Starr, 1990: Is there a cirrus small particle radiative anomaly? Conference on Cloud Physics, San Francisco, CA, AMS, Boston, Mass.
- Wielicki, B.A., J.T. Suttles, A.J. Heymsfield, R.M. Welch, J.D. Spinhirne, M. Wu, D. Starr, L. Parker, and R.F. Arduini, 1990: The 27-28 October 1986 FIRE IFO cirrus case study: Comparison of Radiative transfer theory with observations by satellite and aircraft. *Mon. Wea. Rev.*, **118**, 2356-2376.

APPENDIX 1

**Table A1:
University of Utah ETO Data Summary Sheet Explanations**

Lidar

Data Rate

- Regular (at maximum 30 s shot rate)
- Monitor (at less than the maximum PRF)
- Scan (elevation angle scanning operations)

Support Data

- Radiation
- Photographic (180° fisheye)
- IR Radiometer (narrow beam midinfrared radiance)
- Microwave Radar (K_a-band radar reflectivity data)

Satellite

- NOAA 9, 10, and 11 platforms

Cloud Conditions (± 15 min. of overpass)

Amounts of high, middle, and low cloud cover, where

- 1 = Overcast (10/10 coverage)
- 2 = Broken (6/10 to 9/10 coverage)
- 3 = Scattered (1/10 to 5/10 coverage)

Types - High

- 1 = Cirrostratus (uniform-appearing)
- 2 = Fibratus (fibrous, streaks, contrails)
- 3 = Spissatus (dense patches, anvils, lenticular)
- 4 = Thin or subvisual cirrus
- 5 = Thick, probably attenuation-limited
- 6 = Ice crystal optical phenomena (haloes, etc.)

Types - Middle

- 7 = ALSt (primarily ice phase)
- 8 = ALCu (cellular or lenticular, water phase dominates)

Types - Low

- 9 = Stratus, fog
- 10 = Cumulus, fractus
- 11 = Cumulus with significant vertical development, Cb
- 12 = Precipitation at site

UNIVERSITY OF UTAH LIDAR ETO DATA SUMMARY

PERIOD: 2 May - 25 June 1990

SITE: Lat. 40° 46' 00" Long. 111° 49' 38"
Elevation 1.520 km MSL

Lidar										Satellite										Cloud Conditions											
		Data Rate								Sup- porting		Over- pass		E S N R A N 1 B G 1				High						Mid.			Low				
Date	Times (GMT)	R	M	S	F	R	P	I	M	(GMT)	9	0	S	E	1	A	1	2	3	4	5	6	A	7	8	A	9	10	11	12	
5/2	0006-0132	X				X	X			0113		X				2		X	X												
5/3	0138-0230	X				X				0230		X				0		X													
*5/10	0301-0739	X				X				0313		X				3		X													
5/14	2055-2225	X				X	X			2102					X	1			X						3		X	X			
5/17	0003-0040	X				X	X									3		X													
	0200-1107	X				X	X			0215		X				3		X													
		X				X				0904					X	1	X	X													
		X				X				1021				X		1	X	X													
		X				X				1045					X	1	X	X													
	2152-2359	X				X	X			2212					X	1		X	X						3		X				
5/18	0001-0015	X				X	X									1		X	X							3		X			
	2039-2310	X				X	X			2201					X	1		X		X						3		X			
*5/20	2111-2337	X				X	X			2140					X	1	X	X								3		X			
*5/21	2114-2359	X				X	X			2129					X	3		X		X						3		X			
*5/22	0001-0028	X				X	X									2		X	X												
*5/23	0256-0424	X				X				0320		X				0				X											
	2025-2152	X				X	X			2108					X	1				X						3		X			
*5/24	0228-0330	X				X				0257		X				1				X				3		X					
*5/25	2011-2120	X				X	X			2046					X	3		X	X					3		X					
5/26	0115-0435	X				X	X			0212		X				1	X	X	X												
5/31	0031-0116	X				X	X																3		X	2		X	X		
	0606-1013	X				X				0601				X		1		X		X											
		X				X				0957					X	1	X														
6/3	2000-2333	X				X	X			2051					X	1	X	X		X											
6/4	1900-1953	X				X										3		X	X												
*6/6	1930-2117	X				X	X			2020					X	2		X	X							3		X			
6/11	2246-2352	X				X	X									3		X	X							3		X	X		
6/12	0135-0344	X				X	X			0229		X				1			X					3		X	2		X	X	
		X				X				0302				X		1			X					3		X					
6/13	2125-2151	X				X	X																								
6/14	0135-0326	X				X	X			0141				X		3		X		X											
		X				X	X			0144		X				3		X		X											
		X				X				0324		X				3		X		X											
6/15	0000-0130	X				X	X			0011				X		2		X	X												
		X				X	X			0122		X				3		X													
*6/21	1602-1910	X				X	X			1622		X				2		X													
	2052-2236	X				X	X			2102					X	3		X													
*6/22	1706-2010	X				X	X									2	X	X		X		X									
*6/25	2150-2305	X				X	X			2200					X	3		X		X						3		X			

*Primary satellite day.

UNIVERSITY OF UTAH LIDAR ETO DATA SUMMARY

PERIOD: 26 June-29 Aug. 1990

SITE: Lat. 40° 45' 17" Long. 111° 49' 10"
Elevation 1.52 km MSL

Lidar										Satellite										Cloud Conditions												
										Over- E S																						
Data Sup-										pass N R A N										High Mid. Low												
Rate porting										Time N 1 B G 1																						
Date	Times (GMT)	R	M	S	F	R	P	I	M	(GMT)	9	0	S	E	1	A	1	2	3	4	5	6	A	7	8	A	9	10	11	12		
6/26	0207-0253	X				X				0213		X				3		X								3		X				
	2132-2219	X				X	X			2150					X	0		X							0		X					
*7/5	2040-2352	X				X	X			2117					X	2		X	X													
*7/7	1730-1917	X				X	X									2		X	X					3		X						
	2103-2359	X				X	X			2056					X	2		X						3		X	3		X			
*7/8	0001-0010	X				X	X									2		X						3		X	3		X			
	0335-0630	X				X						?				1		X														
*7/10	0022-0307	X				X	X			0120		X				2		X	X							2		X	X			
		X				X	X			0300		X				2		X	X							3		X	X			
7/17	0410-0608	X				X										2		X	X													
	1836-2359	X				X	X		X	2047					X	2		X	X							3		X	X			
7/18	0000-0026	X				X	X		X							2		X							2		X	X				
7/29	0150-0359	X				X	X			0248		X				2		X							3		X					
7/31	0130-0330	X					X			0140		X				3		X	X						3		X					
		X								0320		X				2		X	X													
8/1	2202-2256	X					X		X							2		X	X							3		X				
*8/8	2245-2359	X					X									2			X							3		X	X			
*8/9	0001-0430	X					X		X	0134		X				2			X							3		X	X			
		X							X	0314		X				1		X	X													
*8/10	2023-2359	X					X		X	2138					X	2		X									3		X	X		
	0001-0015	X					X		X																							
	1500-1724	X					X			1507		X				2		X		X												
	2104-2359	X					X		X	2138					X	1	X	X	X					3		X	3		X	X		
8/11	0721-0841	X														?		X	X													
8/13	0115-0610	X					X			0143		X				1	X	X	X													
		X								0323		X				2		X	X													
	1510-1625	X					X			1539		X				1	X	X		X												
8/15	1609-1722	X					X			1633		X				1		X						2		X	3		X			
8/19	1934-2359	X					X			1949					X	1		X	X	X						2		X	X			
		X					X			2129					X	1	X		X							3		X	X			
*8/20	0001-0011	X					X									1	X		X					2		X	3		X			
	2003-2132	X					X			2118					X	2	X	X	X					3		X	3		X	X		
*8/22	2051-2359	X				X	X		X	2057					X	3		X	X					3		X	3		X			
*8/23	0001-0356	X				X	X			0115		X				3		X	X													
		X				X	X			0254		X				3		X														
8/26	0227-0815	X				X			X	0326		X				1	X	X	X													
8/28	0145-0345	X				X				0240		X				2		X	X													
	1730-1852	X				X	X		X							1	X	X	X				X									
	1956-2351	X				X	X		X	2132					X	1	X	X					X									
8/29	0200-0313	X				X	X		X	0217		X				1	X	X														

*Primary satellite day.

UNIVERSITY OF UTAH LIDAR ETO DATA SUMMARY

PERIOD: 1 Sept. - 15 Oct. 1990 SITE: Lat. 40° 46' 00" Long. 111° 49' 38"
Elevation 1.52 km MSL

Lidar										Satellite						Cloud Conditions															
		Data Rate				Sup- porting				Over- pass		N R A N 1 1 B G 1					High						Mid.			Low					
Date	Times (GMT)	R	M	S	F	R	P	I	M	(GMT)	9	0	S	E	1	A	1	2	3	4	5	6	A	7	8	A	9	10	11	12	
9/1	2042-2359	X				X	X			2048					X	1	X	X		X		X	3		X	3		X			
9/2	0001-0640	X				X			X	0226		X				1		X							3		X				
	1952-2046	X				X	X			2037					X	1		X	X						3		X	2		X	X
9/4	0122-0406	X				X	X		X	0140		X				1		X	X					3		X					
		X				X			X	0320		X				1		X	X					?		?				X	
* 9/5	1836-2200	X				X	X			2005					X	1		X	X					3		X	3		X		
		X				X	X			2145					X	1		X	X					3		X	2		X	X	
* 9/8	0310-0709	X				X				0328		X				?		X	X												
9/11	0350-0451	X				X																									
9/15	2236-2359	X				X	X		X							1		X	X					3		X	3		X		
9/16	0000-0425	X				X			X	0205		X				1		X	X							3		X	X		
9/17	2241-2359	X				X	X		X							1		X	X												
9/18	0001-0321	X				X	X		X	0120		X				2		X	X												
		X				X			X	0300		X				?		X	X												
* 9/24	1823-2110	X					X			1959					X	2		X		X						3		X	X		
* 9/25	0142-0326	X								0200		X				2		X	X												
	2107-2359	X					X			2128					X	2		X	X							2		X	X		
9/26	0001-0320	X							X	0137		X				1		X	X							2		X	X		
		X							X	0317		X				1			X							2		X	X		
	2057-2300	X							X	2117					X	1		X	X							3		X			
9/27	1806-2218	X				X	X		X	2106					X	1		X	X							3		X	X		
10/2	0703-0846	X				X										3		X													
	1826-2023	X				X	X		X	2012					X	2		X	X												
*10/5	1922-2245	X				X	X		X	2120					X	1	X		X	X						3		X			
*10/6	0051-0318	X				X	X		X	0109		X				1	X				X					3		X			
		X				X			X	0248		X				1	X	X	X							3		X			
*10/9	1806-2219	X				X	X			2036					X	3		X		X											
		X				X	X			2217					X	3		X		X											
*10/10	0110-0315	X				X	X			0117		X				2		X													
			X			X				0257		X				?															
10/11	0221-0345	X				X				0234		X				?		X						?		X					
	1756-2208	X				X	X		X	2014					X	1	X	X				X									
		X				X	X			2155					X	3	X	X													
10/12	1706-2008	X				X	X		X	2004					X	2	X	X													
	2127-2359	X				X	X			2144					X	1	X	X													
10/13	0001-0017	X				X	X									2	X	X													
	0545-0857	X				X	X		X																						
	1536-1628	X				X	X			1544		X				1	X							2		X					
10/15	0230-0330	X				X				0242		X				?		X													

*Primary satellite day.

UNIVERSITY OF UTAH LIDAR ETO DATA SUMMARY

PERIOD: 4 Nov. - 4 Dec 1990

SITE: Lat. 40° 46' 00" Long. 111° 49' 38"
Elevation 1.52 km MSL

Lidar										Satellite						Cloud Conditions															
		Data Rate				Sup- porting				Over- pass Time		E S N 1 B G 1					High						Mid.			Low					
Date	Times (GMT)	R	M	S	F	R	P	I	M	(GMT)	9	0	S	E	1	A	1	2	3	4	5	6	A	7	8	A	9	10	11	12	
11/4	1900-2335	X				X	X			2046					X	1	X	X					1	X	X						
*11/9	2045-2359	X				X	X			2131					X	1	X			X											
*11/10	0100-0412	X				X				0108		X				1	X			X											
		X				X				0249		X				?				X											
11/11	0407-0441		X													?															
11/12	2035-2256	X				X	X		X	2057					X	1		X													
11/13	2335-2359	X				X	X									1	X	X	X												
11/14	0000-0329	X							X	0117		X				1	X	X	X												
		X				X				0257		X				?	X														
	1925-2251	X				X	X		X	2035					X	1			X												
		X				X	X		X	2216					X	1			X												
11/15	0415-0605	X				X										?		X													
*11/22	0116-0338	X				X				0134		X				?		X					?		X						
		X				X				0314		X				?	X						2		X						
*11/23	0033-0837	X				X				0111		X				?		X													
		X				X				0251		X				?	X														
*11/24	0024-0054	X				X										3		X												X	
11/30	0001-0410	X				X				0151		X				?	X	X	X				?		X						
	0914-1202	X				X			X	0932					X	1	X														
		X				X			X	1113					X	1	X														
12/4	0014-0137	X				X				0150		X				?	X			X											

*Primary satellite day.

Report No. 21

UNIVERSITY OF UTAH LIDAR ETO DATA SUMMARY

PERIOD: 7 Feb - 27 Mar 1991

SITE: Lat. 40° 46' 00" Long. 111° 49' 38"
Elevation 1.52 km MSL

Lidar										Satellite										Cloud Conditions															
		Data Rate				Supporting				Over-	E S					High						Mid.			Low										
Date	Times (GMT)	R	M	S	F	R	P	I	M	pass Time (GMT)	N	1	R	A	N	N	1	B	G	1	A	1	2	3	4	5	6	A	7	8	A	9	10	11	12
*2/7	0106-0415	X				X				0155		X									?		X		X										
	2104-2207	X				X	X			2138					X						2		X		X										
*2/8	0116-0318	X				X				0132		X									2		X												
		X				X				0312		X								?															
2/12	0105-0605	X				X				0140		X									1		X		X										
		X				X				0320		X								?				X											
	1507-1752	X				X	X			1536		X									1		X		X										
	2209-2302	X				X	X	X		2223					X						1		X	X		X		3		X					
2/15	1958-2359	X				X	X	X		2009					X						1		X		X				2		X				
		X				X	X	X		2150					X						1		X	X	X										
2/16	0001-0015	X				X	X	X																											
	0131-0337	X						X		0148		X									1	X			X				3		X				
2/18	2014-2240	X				X	X	X		2116					X						2		X		X						3		X	X	
*2/20	0051-0543	X				X		X		0156		X									1	X		X					3		X				
2/28	0103-0626	X						X		0211		X									1	X	X		X										
3/3	0048-0311	X				X	X	X		0103		X									1		X	X	X				3		X				
*3/5	0435-0526	X				X		X													?				X						2		X	X	
*3/7	0247-0313	X						X		0251		X									?								?		?		X	X	
*3/9	2033-2359	X				X	X	X		2107					X						1	X	X												
*3/10	0001-0405	X				X		X		0142		X									1	X	X												
		X				X		X		0322		X									1	X													
	2017-2310	X				X	X	X		2055					X						1	X					X					3		X	
3/12	2000-2215	X				X	X	X		2033					X						1	X	X				X	3		X	3		X		
		X				X	X	X		2214					X						2				X	X			3		X	3		X	
3/13	0118-0418	X				X		X		0150		X									3		X												
	1610-1806	X				X		X													1	X					X	3		X					
3/15	0200-0457	X				X		X		0307		X									?				X						?	X	X		
3/17	2051-2357	X				X	X	X		2118					X						1		X		X						3		X		
3/18	0137-0540	X				X		X		0157		X									1	X	X		X										
	1629-1732	X				X	X	X													1	X	X		X										
*3/20	2025-2248	X				X	X	X		2045		X									3		X						3		X	3		X	X
		X				X	X	X		2226		X									2		X	X							3		X		
*3/21	0117-0245	X				X		X		0228		X									?	X	X												
*3/23	0233-0440	X				X		X		0323		X									?				X				2		X				
	1520-2220	X				X	X	X		1538		X									1	X					X		2	X					
		X				X	X	X		2012					X						1	X	X	X											
		X				X	X	X		2152					X						1	X	X	X											
*3/25	0110-0410	X						X		0236		X									1	X	X				X		3		X				
3/26	1818-1852	X				X	X	X													1	X							2	X		3		X	X
3/27	0447-0607	X				X		X													?				X			3		X					

*Primary satellite day.

UNIVERSITY OF UTAH LIDAR ETO DATA SUMMARY

PERIOD: 30 March - 26 May 1991 SITE: Lat. 40° 46' 00" Long. 111° 49' 38"
Elevation 1.52 km MSL

Lidar										Satellite						Cloud Conditions															
		Data Rate				Sup- porting				Over- pass Time	E S N R A N					High						Mid.			Low						
Date	Times (GMT)	R	M	S	F	R	P	I	M	(GMT)	9	0	S	E	1	A	1	2	3	4	5	6	A	7	8	A	9	10	11	12	
3/30	0223-0535	X				X		X		0221		X				2		X		X						3		X			
3/31	1946-2252	X				X	X	X		2024				X		1	X	X													
		X				X	X	X		2204				X		1	X	X					X								
4/2	2123-2208	X				X	X	X		2142				X		2	X	X		X											
4/3	0143-0256	X				X	X	X		0229		X				1	X						3		X						
4/4	0130-0440	X				X	X	X		0206		X				2		X		X											
	1513-1710	X				X	X	X		1602		X				1	X	X		X											
	0101-0327	X				X	X	X		0143		X				1	X	X	X												
*4/5	2028-2315	X				X	X	X		2109				X		1	X		X												
	0104-0625	X				X	X	X		0121		X				1	X														
*4/6		X				X		X		0300		X				1	X			X											
		X				X		X		0121		X				1	X														
*4/9	2003-2214	X				X	X	X		2024				X		1	X					X	3		X						
		X				X	X	X		2205				X		1	X						3		X	3		X			
*4/10	0104-0430	X				X	X	X		0129		X				1	X						2	X		3		X			
		X				X		X		0309		X											1	X							
4/14	0041-0323	X				X	X	X		0137		X				2	X						2		X	3		X			
		X				X		X		0317		X											1		X						
	2030-2322	X				X	X	X		2109				X		1	X	X													
4/17	0200-0459	X				X	X	X		0208		X				2		X		X											
4/19	0104-0306	X				X	X	X		0121		X				2		X		X											
		X				X		X		0301		X				?				X											
	1518-1720	X				X	X	X		1518		X				1	X	X		X											
	1951-2215	X				X	X	X		2014				X		1	X	X		X											
		X				X	X	X		2155				X		1	X			X					3		X				
*4/20	0220-0545	X				X	X	X		0238		X				1	X			X											
*4/22	0120-0514	X				X	X	X		0152		X				1	X	X	X				3		X						
*4/24	1651-1811	X				X	X	X								1	X						2		X						
5/4	0207-0510	X				X	X			0216		X				2	X	X					3		X						
*5/5	2135-2332	X				X	X			2218				X		1	X	X				X									
*5/6	0120-0409	X				X	X			0130		X				1	X	X													
		X				X				0310		X				1	X	X													
*5/7	1931-2224	X				X	X			2016				X		1	X	X		X		X	3		X						
		X				X	X			2156				X		1	X	X	X												
5/13	1554-1933	X				X	X			1605		X				1	X	X	X												
		X				X	X	X		2049				X		1	X	X					3		X						
		X				X	X	X		2230				X		1	X						1	X							
5/17	1606-1711	X				X	X	X		1613		X				3	X			X						3		X			
*5/25	0215-0450	X				X	X	X		0233		X				1	X	X	X												
		X				X	X	X		2157				X		2		X	X							3		X	X		
5/26	0002-0232	X				X	X	X		0210		X				2		X	X							3			X		

*Primary satellite day.

Corona-producing cirrus cloud properties derived from polarization lidar and photographic analyses

Kenneth Sassen

Polarization lidar data are used to demonstrate that clouds composed of hexagonal ice crystals can generate multiple-ringed colored coronas. Although relatively uncommon in our mid-latitude cirrus sample (derived from Project FIRE extended time observations), the coronas are associated with unusual cloud conditions that appear to be effective in generating the displays. Invariably, the cirrus cloud tops are located at or slightly above elevated tropopauses (12.7-km MSL average height) at temperatures between -60° and -70°C . The cloud top region also generates relatively strong laser backscattering and unusually high 0.5–0.7 linear depolarization ratios. Color photograph analysis of corona ring angles indicates crystals with mean diameters of from 12 to 30 μm . The cirrus cloud types were mainly subvisual to thin (i.e., bluish-colored) cirrostratus, but also included fibrous cirrus. Estimated cloud optical thicknesses at the 0.694- μm laser wavelength ranged from ~ 0.001 to 0.2, where the upper limit reflects the effects of multiple scattering and/or unfavorable changes in particle characteristics in deep cirrus clouds.

I. Introduction

The corona is a diffraction phenomenon that, in its most spectacular form, is manifested by a concentric series of three or four brilliantly colored rings about the sun or moon. In its simplest form, the corona (literally a crown) is represented by the aureole (or halo of the magical religious variety), which is a white disk bordered near the sun or moon by a bluish ring and terminated by a reddish-brown band. Iridescence is a related display whose patches of brilliant color, usually seen at relatively large angular separations from the sun, can be considered as fragments of corona rings. To obtain a unified understanding of these phenomena, it is only necessary to consider basic diffraction theory and have general knowledge of the microphysical contents of the clouds causing the displays.¹ According to simple diffraction theory, the purest effects are produced by monodispersed particle sizes, with the radius of any particular order of colored rings increasing with decreasing particle size. Thus, aureole may be produced by relatively large particles

that tightly compress the rings, or by the presence of a broad particle size distribution that causes the colored rings to overlap; corona by appropriately sized and uniform particles that provide for a favorable angular separation of the colored rings; and iridescence by spatially restricted groups of relatively small uniform particles, as near the edges of growing or evaporating clouds.

Although these factors controlling diffraction phenomena in clouds are reasonably well understood, the nature of the cloud particles causing the displays has been the subject of controversy. As discussed, for example, by Humphries,² the fact that brilliant coronas were often seen in high clouds, whose temperatures must have been far below freezing, prompted early investigators to conclude that not only spherical cloud droplets, but also ice crystals must be responsible for coronas. In view of these reports, Minnaert³ was compelled to treat the case for a corona from ice needles in terms of a diffraction pattern for a slit. However, it is now well established that small water droplets can be supercooled to temperatures approaching approximately -40°C in the middle and upper troposphere, while ice crystals can assume a variety of shapes and orientations that are hardly conducive to generating pure coronal colors. This evidence led various investigators^{1,2,4} to speculate that corona from ice clouds should be rare, if not nonexistent. However, to settle this issue properly, an experimental approach that measures the content of corona-producing high clouds is clearly needed. Based on the results of just such a

The author is with University of Utah, Meteorology Department, Salt Lake City, Utah 84112.

Received 3 October 1990.

0003-6935/91/243421-08\$05.00/0.

© 1991 Optical Society of America.

program, it is demonstrated here that cirrus ice crystal clouds can indeed generate brilliant corona displays.

II. Experimental Program and Methods

The measurements described here have been collected as part of a comprehensive cirrus cloud research program in connection with the University of Utah Extended Time Observation (ETO) component of Project FIRE (the First International Satellite Cloud Climatology Program Regional Experiment). The approaches used to study cirrus clouds in our program include remote sensing with polarization ruby lidar (0.694- μm wavelength), passive radiometry, and frequent all-sky and normal cloud photography. These ETO measurements have now been regularly collected for over a 3-yr period from our facility in Salt Lake City, Utah, and similar data were also obtained from a site in central Wisconsin during the October–November 1986 FIRE Intensive Field Observation (IFO) experiment.

One goal of our research plan is to photograph and examine the kinds and frequencies of cirrus cloud optical phenomena, including corona, and then relate each display to the cirrus cloud composition and physical properties derived from concurrent lidar polarization data. The lidar determines the height and thickness of the cirrus, and by means of the linear depolarization ratio (δ , the ratio of the backscattered powers in the planes of polarization perpendicular and parallel to that of the laser), a measure of the composition of the cloud.⁵ For example, δ values in cirrus normally range from ~ 0.3 to 0.5 , which reflect differences in the habits of the ice crystals present (that are unfortunately still only poorly understood), but $\delta \approx 0$ are also sometimes observed. These low values are caused by either supercooled cloud droplets or fields of horizontally oriented planar ice crystals within cirrus. (Unambiguous water cloud discrimination is still possible, however, since the strong crystal specular reflections diminish markedly when the lidar is scanned a few degrees off the zenith direction.) It is not possible to point the lidar system close to the sun, where the corona occurs, because of the extreme level of background radiation, but it is usually possible to determine whether the same cloud volume has been sampled by considering the distribution and movement of the clouds under study.

Another product derived from the lidar data is the estimated cloud optical thickness τ at the ruby laser wavelength. The method relies on a clear air lidar calibration below the cirrus cloud base and specifies the values of lidar equation terms on the basis of ice crystal ray-tracing simulations. As in our recent lidar analysis of a corona-generating cirrus cloud, which yielded results in reasonable agreement with ground-based radiometric information,⁵ we use here the values of the backscatter-to-extinction ratio $k = 0.075$ and the multiple scattering correction factor $\eta = 0.65$. The basic uncertainty in τ is about a factor of 2, based on the usual range of scattering factors for randomly oriented simple ice crystals. Data averages of ten data

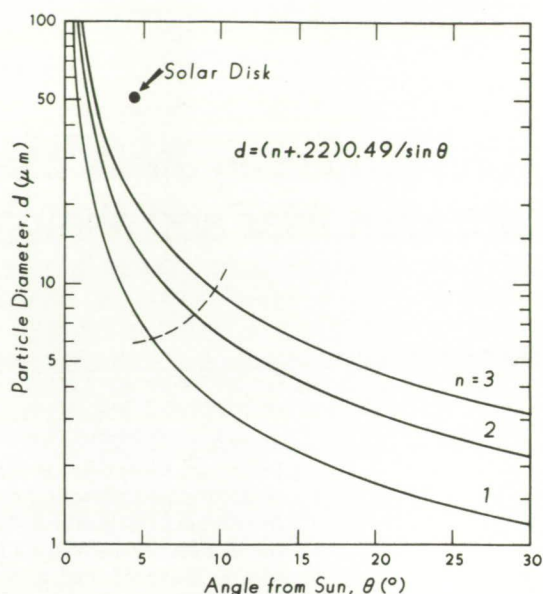


Fig. 1. Plot of the dependence of corona red ring radii of order $n = 1$ – 3 on spherical particle diameter, derived from simple diffraction theory [Eq. (1), inserted]. The relative size of the solar (or lunar) disk, which precludes corona formation from large particles, and the approximate onset of anomalous diffraction (dashed curve), which interferes with corona formation from small water spheres, are indicated.

points (75 m) in the vertical and ten consecutive shots (typically 5 min) are used here to compute τ .

As in a previous study,¹ color corona photographs are analyzed through the use of the following expression derived from simple diffraction theory:

$$\sin \theta = (n + 0.22)\lambda/d, \quad (1)$$

which relates the angular position θ from the sun of a corona minima of order n at wavelength λ to the cloud particle diameter d . Previously, a $\lambda = 0.57 \mu\text{m}$ has been used to determine the positions of the corona red bands under the assumption that the red rings would be most vivid at the angular positions corresponding to the minima for diffracted green light.² However, a recent reevaluation of the corona on the basis of Mie theory and chromaticity considerations⁶ found, as expected,^{7,8} discrepancies in using the simple diffraction approach. Simple diffraction theory naturally fails to account for the effects of anomalous diffraction, which result from the interference between rays that are diffracted around and transmitted through relatively small cloud droplets, but also overestimates the droplet diameter somewhat when $\lambda = 0.57 \mu\text{m}$ is inserted in Eq. (1). Therefore, we have used a $0.49\text{-}\mu\text{m}$ wavelength to be in compliance with their findings. Figure 1 provides the expected relationship between spherical particle diameter and the angular separations of the first three orders of the corona red bands. Recognizing that cirrus cloud particles are not likely to be either monodispersed in size or spherical in shape, however, we derive from Eq. (1) the mean characteristic particle diameter \bar{d} .

III. Experimental Results

A. Case Studies

One cirrus cloud observational program is ongoing, but to this time nine ETO data sets of multiple ringed corona displays have been obtained. Considering that a few hundred cirrus observation periods (each typically of 1–3-h duration) are represented, it can be concluded that coronas in the cirrus of our region are relatively rare, although it should be noted that a larger number of transient and poorly developed aureole, corona, and iridescence displays have been observed in cirrus. In addition, during the 1986 FIRE IFO experiment a zenith subvisual cirrus cloud that generated colored corona rings was studied,⁵ which brings the total sample to ten separate occurrences of solar and lunar coronas.

To evaluate the cirrus cloud conditions associated with corona generation, ETO data sets for the five solar and four lunar corona displays are provided in Fig. 2. For each ETO case study are given 2- or 3-h height versus time displays of lidar relative range-normalized returned power P and linear depolarization ratio δ , from which cirrus cloud structure and composition can be inferred, along with temperature profiles derived from local sounding data. Sample color images of the coronas and all-sky fisheye photographs of the cirrus are provided in Figs. 12(a)–12(d) and 3. Note that the corona photographs were selected for inclusion here on the basis of their journal reproducibility, whereas less striking images were still suitable for analysis. The color figures were obtained from rather long-lived corona displays in extensive cirrostratus, such that particularly valid comparisons between the zenith-pointing lidar and the corona photographs (taken with the sun or moon at various elevation angles) can be expected. In almost all cases, the lidar appears to have viewed the corona-producing cirrus regions within 10–20 min of the corona observations, based on radiosonde wind data. Brief descriptions of each case study data set are provided below.

20 Oct. 1988 The 2-h zenith lidar displays (see figure caption for times) of returned power (left of each pair) and linear depolarization ratio in Fig. 2(a) show the passage of several fibrous cloud bands. The generating level of the cirrus particles extends to the tropopause height (TP in the temperature profile at right). The range of depolarization ratios is unusual for cirrus. Particle fall streaks displaying both relatively high 0.6–0.7 and low ≤ 0.15 δ values are present (see figure caption for δ value symbol key). The latter values are caused by the specular reflections from horizontally oriented planar ice crystals, but the cause of the high depolarizations is uncertain. Only one incomplete solar corona within a narrow fibrous cloud band was photographed (as shown by the arrow in the P display), and unfortunately this cloud region was not sampled by the lidar. Analysis of the photograph yielded a mean particle diameter $\bar{d} = 17 \mu\text{m}$.

6 Apr. 1989 The thin cirrostratus, which contained

numerous contrails and may have been contrail-generated, appeared bluish and was often barely visible to subvisual in the zenith viewing direction [see fisheye photograph in Fig. 3(a)]. The lidar data [Fig. 2(b)] show two scattering layers—the lower discontinuous layer generated typical cirrus δ values, but the upper layer, which extended to the tropopause, contained mostly 0.5–0.6 values that are somewhat high for cirrus. Three similar corona photographs [see, e.g., Plate 12(a)] were obtained from the subvisual to very thin cirrostratus early in the period, and yielded an average $\bar{d} = 15 \mu\text{m}$. Weakly colored coronas were also later observed. Estimated cloud optical thicknesses τ varied over the 0.01–0.04 range bracketing the $\tau \approx 0.03$ visible threshold reported for cirrus.⁵

9 Jan. 1990 A cirrostratus overcast containing dense streaks and generating cell complexes gradually advected through the area. Fibrous cirrus cloud bands along the trailing edge of the cirrus mass generated mostly incomplete corona rings, from which a $\bar{d} = 24 \mu\text{m}$ has been derived. The lidar data [Fig. 2(c)] illustrate the thinning of the cirrus layer from a 2–3-km depth ($\tau \approx 0.2$) to a thickness of ≤ 1.0 km in the fibratus producing the corona ($\tau \approx 0.01$ –0.03). Lidar depolarization is unusually high in the tropopause-based upper cloud region and gradually decreases toward cloud base.

8 Mar. 1990 Lunar corona were observed during two periods [Figs. 2(d) and 2(e)] on this occasion. Typically, a strongly scattering cloud top layer at the tropopause was present, and particles trailing from this generating level formed a cirrostratus 2.5–4.0 km in thickness. As in the above case, depolarization was unusually high in the upper cirrus and tended to decrease below, although the mostly $\delta \approx 0.5$ values in the lower cloud are still somewhat high for typical cirrus. During the first period [Fig. 2(d)], aureole and weakly colored corona were intermittently observed and stars were usually visible through the overcast, with τ ranging widely from 0.01 to 0.25. (None of these photographs proved suitable for analysis.) Lunar corona were observed only during the initial part of the second period [Fig. 2(e)], when stars were again visible. The corona photograph of 0809 yielded $\bar{d} = 13 \mu\text{m}$. By 0820, however, the corona and stars had disappeared because of the rapid thickening of the cirrus cloud system, and τ increased from ~ 0.05 to 0.25.

4 Apr. 1990 Although the corona photographs proved only marginally suitable for analysis, this cirrus cloud system [Fig. 2(f)] is particularly interesting in that both lunar corona and 22° halo displays were noted. Two cirrus layers were often present, and it is likely that both resulted from spreading anvils caused by local convective activity. The top layer displays several horizontal layers and strongly depolarizing cloud top features that protrude into the lower stratosphere. Comparison of the δ values within the two cirrus layers demonstrates the unusually high depolarizations in the tropopause cirrus layer. Note that the complete but weakly colored 22° halo was observed only during the appearance of the strongly scattering

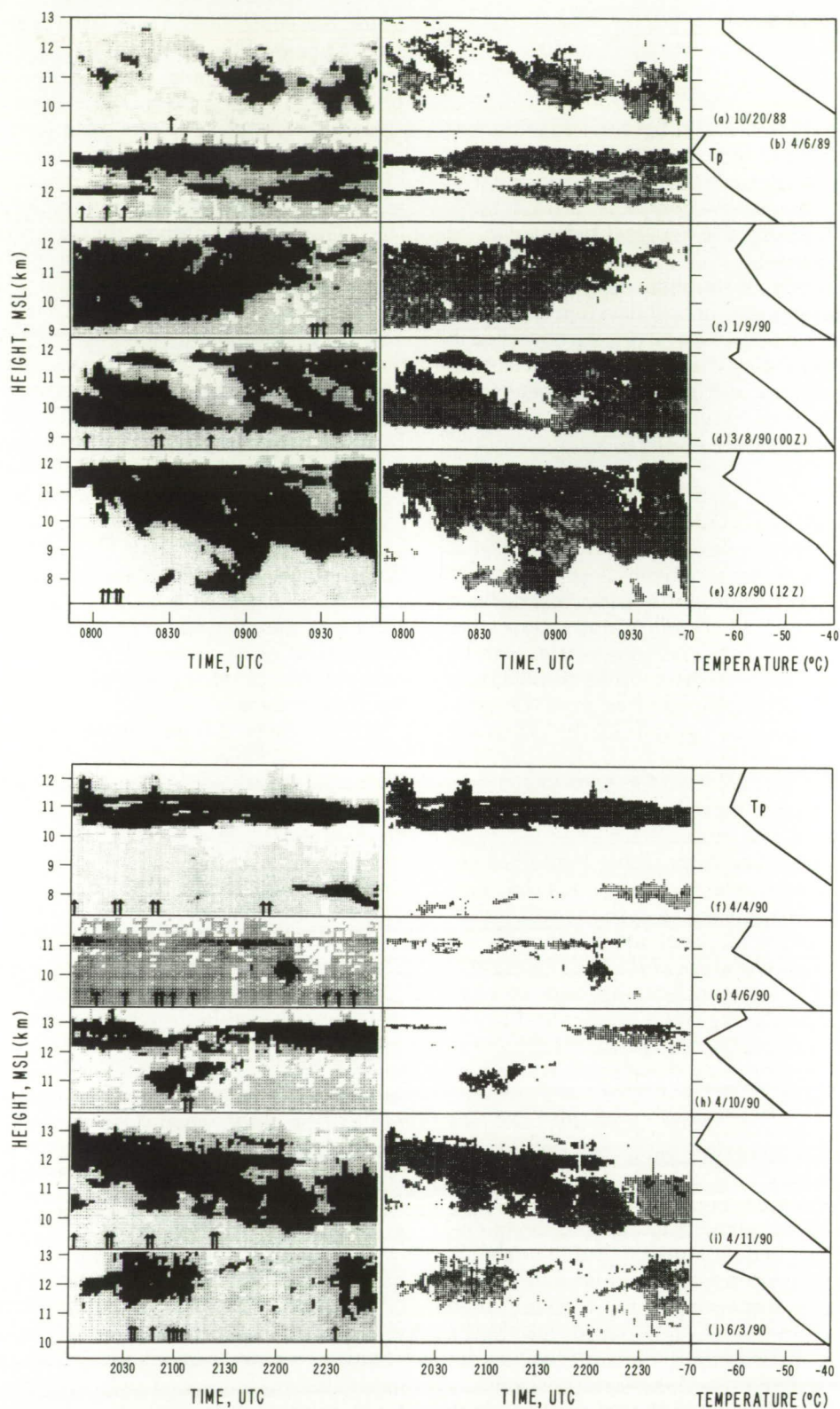


Fig. 2. Height versus time displays of polarization lidar data, along with generally concurrent temperature sounding data, from each of the corona-producing cirrus case studies on the indicated dates. Left of each pair shows a gray scale display of the log of range-normalized returned laser power (where the strongest returns in each plot are shaded black, and lighter shadings occur at -4.86 -dB intervals of the peak value), and linear depolarization ratios are shown at right according to the following symbol key: \blacksquare , $\delta < 0.15$; \bullet , $0.15-0.24$; \div , $0.25-0.34$; $-$, $0.35-0.44$; \times , $0.45-0.54$; \star , $0.55-0.64$; and \blacktriangle , $0.65-0.80$. (Typical cirrus would encompass the \div , $-$, and \times symbols, whereas the star and triangle symbols indicate unusually high depolarizations for cirrus.) The time scales shown apply only to the bottom display in each of the two parts; the times of the other panels are (a) 2230-0130, (b) 2210-0010, (c) 2040-2240, (d) 0300-0500, (f) 0320-0520, (g) 2030-2330, (h) 0500-0700, and (i) 0500-0700. Vertical arrows in the returned laser power displays indicate the times that corona photographs were taken.

layer in the middle of Fig. 2(f) (left). This finding suggests that different ice crystal types may have been responsible for the halo and corona displays, or simply that an increase in cloud optical thickness was needed to generate the halo. Corona particle diameter estimates of $\sim 30 \mu\text{m}$ follow from photographic aureole analyses. Stars were dimly visible over most of the period, with τ generally ranging from ~ 0.1 to 0.2 .

6 Apr. 1990 A 3-h record of the subvisual ($\tau \approx 0.001$ – 0.01) cirrostratus layer is shown in Fig. 2(g). Contrail spreading may have contributed to cirrus formation in this case as well [Fig. 3(b)]. The coronas [see Plate 12(b)] were typically observed in cirrus that would have been invisible were it not for the corona itself and bright solar forward scattering (as also reported in Ref. 5). The lidar backscattering from the ~ 250 -m deep cloud layer above the tropopause was quite weak, often below the threshold used here to calculate δ values (to reduce data digitizing errors). The amount of depolarization measured appears to be typical of cirrus. Corona analysis of three of the photographs yields an average $\bar{d} = 22 \mu\text{m}$. Field notes indicate that three-ringed coronas were sometimes present.

10 Apr. 1990 Lunar aureole and occasional coronas were noted in a very weakly scattering (maximum $\tau \approx 0.01$) cirrostratus layer straddling the tropopause. At sunset this cirrus contained numerous contrails, and so the layer may have been due to contrail spreading. The only photographs attempted were obtained when a lower cirrus cloud was present overhead [Fig. 2(h)], although it is uncertain whether this cirrus contributed to the display from the just-risen moon. Lidar depolarization usually appears to have been rather high at both cirrus altitudes. Unfortunately, the photographs of the weak coronas were unsuitable for analysis. Stars were clearly seen overhead during this display.

11 Apr. 1990 Variable lunar corona effects were observed in the cirrus overcast, through which some stars were dimly visible. Figure 2(i) shows a thickening cirrus cloud that was initially generated at the tropopause height. The δ values in this cirrus are again atypically high, except for near the end of the period when low δ values (≤ 0.25 from oriented planar crystals) developed within the lower cloud region. (No coronas were observed at that time.) Photographic corona analyses indicate a $\bar{d} = 19 \mu\text{m}$ in association with a two-ringed corona, and a $\bar{d} \approx 28 \mu\text{m}$ in a three-ringed corona (based only on aureole analysis). Estimated τ ranged from 0.05 to nearly 0.2 .

3 June 1990 The 3-h period depicted in Fig. 2(j) shows two fibrous cirrus cloud masses embedded in a very thin cirrostratus overcast [see Fig. 3(c)]. Each of these cirrus fibratus ($\tau \approx 0.03$ – 0.04) produced a three-colored ring corona display, although of different radii [Plates 12(c) and 12(d)]. Relatively high lidar δ values of 0.5 – 0.6 are found particularly in the upper cloud region close to the tropopause. The corona photographs yielded $\bar{d} = 22$ and $12 \mu\text{m}$ for the first and second cloud masses, respectively.

B. Mean Properties

Table I and Fig. 4 summarize the physical and microphysical properties of the clouds that have been found to generate coronas. Despite the diversity of cirrus cloud types, it is clear that the cloud heights and temperatures fall within a relatively narrow domain for cirrus. The average cloud top height of 12.7 km and temperature of -65°C will likely prove to be considerably higher and colder than our complete cirrus cloud sample (still being collected). The average midcloud height of 11.7 km is already indicated to be much higher than the normal cirrus heights in our geographic region. The vertical depths of the cirrus during corona displays, plotted against the tropopause (i.e., approximate cloud top) temperature, are shown as the vertical lines in Fig. 4.

The lidar-derived estimates of cloud optical thickness in the cirrus suggest that corona are possible over a rather broad range of τ . Corona displays were noted in cirrus that would otherwise have been invisible to the unaided eye, with τ ranging from ~ 0.001 to 0.01 . The threshold of $\tau \approx 0.03$ determined previously for visible versus zenith subvisual cirrus⁵ is in general agreement with our current findings, although it should be acknowledged that similar assumptions in the lidar analysis were relied on in both studies. An upper limit of $\tau \approx 0.2$ for corona displays is suggested by our current data from cirrus of variable thickness. We have noted during nocturnal observations that the visibility of bright stars near the zenith also tends to disappear when $\tau \gtrsim 0.2$.

Concerning the derived sizes of the ice particles, estimates of the mean particle diameters are compiled in Table I. The values range from 12 to $30 \mu\text{m}$ in the cirrus studied, with an average value of $20 \mu\text{m}$. The plot of mean diameters versus tropopause temperature in Fig. 4 does not indicate any temperature dependence on \bar{d} .

Table I. Physical and Inferred Microphysical Characteristics of the Cirrus Clouds Observed to Generate Two- and Three-Ringed Coronas

Date	Height km MSL	T_p $^\circ\text{C}$	\bar{d} (μm)	Cirrus cloud type
10/21/86	11.7–12.7	–70.1	22	Zenith subvisual band
10/20/88	10.5–12.8	–63.3	17	Cirrus fibratus
4/6/89	11.9–13.4	–70.5	15	Thin cirrostratus
1/9/90	10.1–12.3	–60.5	24	Cirrus fibratus
3/8/90*	9.4–12.1	–62.7	13	Cirrostratus
4/4/90**	10.8–12.4	–61.3	~ 30	Anvil cirrostratus
4/6/90	10.8–11.5	–61.9	22	Zenith subvisual cirrostratus
4/10/90*	10.5–13.1	–67.3	—	Cirrostratus
4/11/90*	10.4–13.3	–69.3	19, ~ 28	Cirrostratus
6/3/90	11.2–13.0	–63.1	12, 22	Fibrous cirrostratus
Average	10.7–12.7	–65.0	20	

* Lunar corona display.

+ Also produced a 22° halo.

Note: Mean particle diameters \bar{d} identified as approximate are based on the lunar aureole radius in photographs that did not preserve the ring positions.

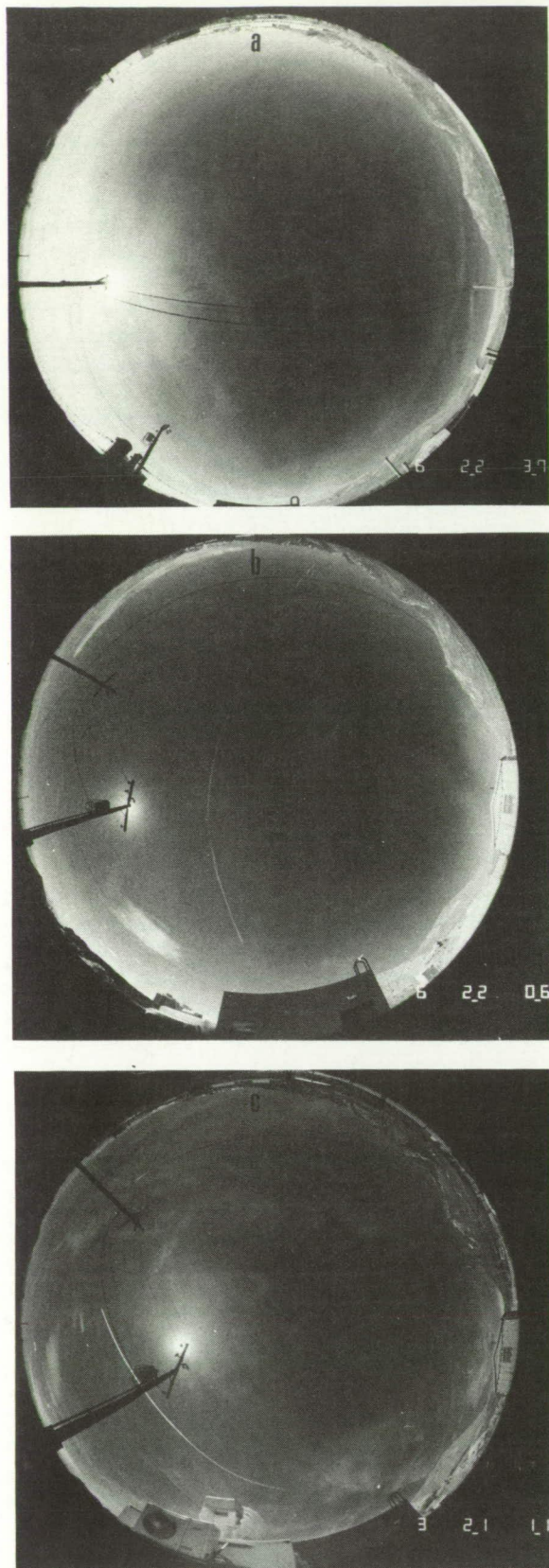


Fig. 3. Representative fisheye photographs obtained at (a) 2237 on 6 Apr. 1989, (b) 2206 on 6 Apr. 1990, and (c) 2111 on 3 June 1990, illustrating the thin to subvisual cirrus cloud conditions usually associated with cirrus coronas. See Plates 12(a)–12(d) for the corona displays generated by these cirrus.

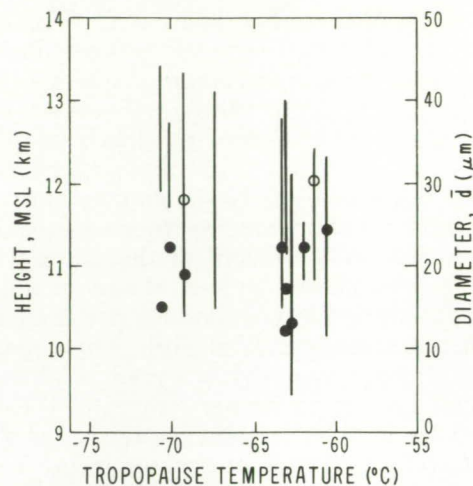


Fig. 4. Summary of lidar-derived corona-producing cirrus cloud heights (vertical lines showing cloud thickness during the displays), and mean particle diameters derived from corona (●) and aureole (○) photographs plotted against tropopause (i.e., approximate cloud top) temperature.

IV. Discussion

The above findings imply that there may be a unique cloud particle shape that is responsible for cirrus corona generation. The range of lidar depolarization produced by these cirrus, on the other hand, indicates that hexagonal ice crystals of some habit or other are responsible. The unusually high (but not unique for cirrus) 0.5–0.7 δ values normally found at the cloud tops represent a signature of populations of this type of ice crystal. In most cases the δ values decreased as the particles descended through the cloud, an indication of a gradual change in particle shape during ventilated growth at warmer temperatures.

The fact that unusually low temperatures are involved in corona-generating cirrus could indicate that crystal growth in this particular habit is favored and/or that the manner in which the particles are nucleated at these great heights leads to populations of small, similar crystals. The results of the corona photographic analyses in Table I illustrate that only a rather narrow range of cirrus particle sizes is involved in corona generation, at least as far as the currently available sample is concerned. Although this additional constraint on cirrus cloud content may simply be a consequence of the laws of diffraction, basic cloud microphysical processes may also help to select particle populations with $\bar{d} \approx 20 \mu\text{m}$. The data points in Fig. 5 for the individual cirrus observations (the * symbols) lie between the zones affected by anomalous diffraction and the convolution effects caused by the angular size of the sun or moon (see Fig. 1). It is unlikely, however, that anomalous diffraction effects analogous to those for spheres⁹ can be produced by ice crystals.

For comparison with the cirrus ice crystal data, given in Fig. 5 as the open circles, are the results of recent analyses of cloud droplet corona displays.⁶ Interestingly, although there is some overlap between the two groups of data, the average particle diameter of $11 \mu\text{m}$

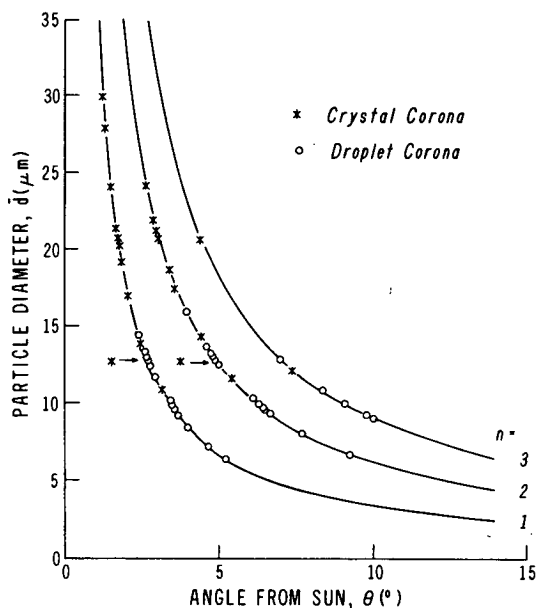


Fig. 5. Comparison of measured corona radii and indicated mean particle diameters for cirrus ice crystal (*) and water droplet (O) (see Ref. 6) clouds.

for droplets is significantly smaller than the 20- μm value for ice crystals. (It should also be noted that lacking auxiliary measurements the droplet corona sample may have included some ice crystal coronas.) This difference probably reflects fundamental cloud microphysical processes acting in the water (i.e., altocumulus and orographic wave) and ice (i.e., high cirrus) clouds capable of generating coronas, and a derived particle diameter of 15 μm may be useful for discriminating between the two types of display. Chromatically, cirrus coronas also typically appear to show more vivid blue rings, in contrast to the dominance of red and greenish colors in droplet coronas, for reasons that remain unclear.

Finally, the preference for cold, high cirrus to occur during certain seasons in our geographic region could account for the large number of springtime corona occurrences (see Table I), although obviously a larger sample will help to assess this climatological aspect.

V. Conclusions

Although infrequently encountered in our mid-latitude cirrus cloud climatological study,¹⁰ several multiple-ringed cirrus corona displays have been documented using polarization lidar and color photographic techniques. The cirrus cloud types involved were primarily zenith subvisual and optically thin cirrostratus that appeared bluish in many viewing directions ($\tau \approx 0.001$ – 0.05), although brief displays from denser and more irregular cirrus were also observed. About one half of the cases were associated with cirrostratus layers 1.5 km or less in depth, in which contrail spreading may have been an important growth factor. Even the thicker and more irregular clouds, however, shared the characteristic of displaying a relatively strongly scattering cloud top layer at the tropopause, which seems

to have been primarily responsible for corona generation. In each case, the clouds occurred at unusually high altitudes and low temperatures for cirrus in our region, averaging 12.7 km and -65°C at cloud top, respectively. Thus it appears to be diagnostic of corona-generating cirrus that they occur in the coldest regions of the upper troposphere extending to and typically slightly above the tropopause. Accordingly, and recognizing that these great altitudes can correspond to the tops of deep mid-latitude cirrus cloud systems,¹¹ multiple scattering in cirrus with $\tau \gtrsim 0.2$ may act to destroy the coronas produced by the cloud top layers, as our observations of cirrus of variable thickness would suggest.

It is significant that the inferred mean sizes of the ice particles in this relatively cold cirrus cloud sample ranged from 12 to 30 μm . Such minute ice crystals are quite unusual for most cirrus,^{12,13} but evidence is accumulating that high, cold ($\lesssim -60^\circ\text{C}$) cirrus clouds contain a significant percentage of relatively small particles, many of which are too small ($\lesssim 50 \mu\text{m}$) even to be detected adequately with available aircraft probes.^{14–16} It appears, therefore, that cirrus ice crystal sizes decrease with decreasing cloud temperature, and this tendency has important implications for radiative transfer through cirrus cloud systems.¹⁷

In one case weak corona and halo displays were noted to occur concurrently within the same cloud. Our understanding of the scattering processes involved in producing the corona and 22° halo suggests that such dual displays are possible. We base this conclusion on findings from laboratory ice cloud scattering research that indicate an ~ 20 - μm lower limit on the sizes of ice crystals that can begin to produce halo effects.¹⁸ As shown here, corona can be produced by ice crystals that somewhat exceed this size, while a relatively broad ice crystal size distribution would also enhance 22° halo formation. If this is indeed the case, the 4 Apr. 1990 case study indicates threshold halo visibility from ice crystals with $\bar{d} \approx 30 \mu\text{m}$.

Although the cirrus temperatures noted here are quite low for mid-latitude clouds, there is no microphysical evidence that unusual types of ice particle, such as spheres or multifaceted (e.g., pyramidal) particles, should dominate at about -60°C . Ice crystals collected from a subvisual cirrus cloud at -83°C , for example, were simple hexagonal crystals with dimensions from ~ 5 to $50 \mu\text{m}$.¹⁹ It was also noted that especially the smaller particles displayed axial ratios of approximately unity, which could contribute to the color purity of coronal rings from nonspherical particles. In view of this evidence and the findings reported here, it is plausible that equidimensional hexagonal ice crystals are involved in cirrus corona generation. We presume that ice crystals of this general type generate the unusually high 0.5–0.7 δ values measured by the lidar. However, the growth of populations of these particles is not necessarily a result of the temperature dependency in ice crystal habit, but may instead be a consequence of the manner in which cirrus clouds are formed at such great heights.

The unique property of these cirrus is that their tops are invariably located at or slightly above the tropopause, that well of frigid air that divides the troposphere and stratosphere. In addition to the extremely low temperatures, this strategic location likely promotes some unusual cloud microphysical processes. For example, ice crystal nucleation may occur from the freezing of haze particles derived from stratospheric particles and tropospheric water vapor. Moreover, the fundamental cloud radiative and microphysical interactions that occur at these great altitudes may contribute to producing the relatively dense cloud top layers.²⁰ Radiative-cooling feedbacks to cloud particle nucleation and growth at the tropopause may hold the key to understanding the conditions associated with corona-forming cirrus.

Note added in proof. More recent FIRE ETO observations have identified five additional cirrus coronas. Four of these occurred during October–November 1990 in association with a synoptic episode of unusually high, subvisual-to-thin cirrus layers. Cloud tops were again located close to the tropopause, with cloud top heights and tropopause temperatures ranging from 12.0 to 15.3 km and -57.5° to -72.5°C , respectively. Overall, the physical and microphysical properties of this additional sample are quite similar to those reported here, lending credence to the narrow range of cirrus properties that can produce coronas, and conversely, to the apparent high frequency of corona occurrences from cirrus located at the tropopause.

The Project FIRE field research and data analysis efforts have been supported by NASA grant NAG-1-868 and National Science Foundation grants ATM-8513975 and ATM-8914348. The author thanks J. A. Lock for his comments and making available the droplet corona data, and A. B. Fraser for suggesting the ice crystal and cloud droplet corona comparison at the recent Topical Meeting on Light and Color in the Open Air.

References

1. K. Sassen, "Iridescence in an aircraft contrail," *J. Opt. Soc. Am.* **69**, 1080–1083 (1979).
2. W. J. Humphries, *Physics of the Air* (McGraw-Hill, New York, 1929).
3. M. Minnaert, *The Nature of Light and Color in the Open Air* (Dover, New York, 1954).
4. G. C. Simpson, "Corona and iridescent clouds," *Q. J. R. Meteorol. Soc.* **38**, 291–299 (1912).
5. K. Sassen, M. K. Griffin, and G. C. Dodd, "Optical scattering and microphysical properties of subvisual cirrus clouds, and climatic implications," *J. Appl. Meteorol.* **28**, 91–98 (1989).
6. J. A. Lock and L. Yang, "Mie theory of the corona," *Appl. Opt.* **30**, 3408–3414 (1991).
7. J. G. Wilson, "Note on optical methods of measuring the size of small water drops," *Proc. Cambridge Philos. Soc.* **32**, 493–498 (1936).
8. Y. G. Naik, "Correlation between optical and dynamic methods of measuring size of water drops in a cloud," *J. Colloid Sci.* **9**, 393–399 (1954).
9. H. C. van de Hulst, *Light Scattering from Small Particles* (Wiley, New York, 1957).
10. Since tropical cirrus frequently form in conditions similar to those reported here, it is possible that cirrus cloud coronas may be relatively more common in tropical and subtropical regions. However, the average $\delta = 0.3$ reported for tropical cirrus (see Ref. 11) is only approximately one half of our value, so it is unclear whether similar particles are present.
11. C. M. R. Platt, J. C. Scott, and A. C. Dilley, "Remote sounding of high clouds. Part VI: Optical properties of midlatitude and tropical cirrus," *J. Atmos. Sci.* **44**, 729–747 (1987).
12. A. J. Heymsfield and C. M. R. Platt, "A parametrization of the particle size spectrum of ice clouds in terms of the ambient temperature and the ice water content," *J. Atmos. Sci.* **41**, 846–855 (1984).
13. K. Sassen, D. O'C. Starr, and T. Uttal, "Mesoscale and microscale structure of cirrus clouds: three case studies," *J. Atmos. Sci.* **46**, 371–396 (1989).
14. C. M. R. Platt, J. D. Spinhirne, and W. D. Hart, "Optical and microphysical properties of a cold cirrus cloud: evidence for regions of small ice particles," *J. Geophys. Res.* **94**, 11,151–11,164 (1989).
15. A. J. Heymsfield, K. M. Miller, and J. D. Spinhirne, "The October 27–28, 1989 FIRE cirrus case study: cloud structure and composition from *in situ* measurements," *Mon. Weather Rev.* **118**, 2313–2328 (1991).
16. K. Sassen, A. J. Heymsfield, and D. O'C. Starr, "Is there a cirrus small particle radiative anomaly?" presented at Conference on Cloud Physics, San Francisco, CA, Preprints available from American Meteorological Society, Boston, Mass.
17. P. Minnis, D. F. Young, K. Sassen, J. M. Alvarez, and C. J. Grund, "The 27–28 October 1986 FIRE IFO cirrus case study: cirrus parameter relationships derived from satellite and lidar data," *Mon. Weather Rev.* **118**, 2402–2425 (1991).
18. K. Sassen and K. N. Liou, "Scattering of polarized laser light by water droplet, mixed phase and ice clouds. Part I: Angular scattering patterns," *J. Atmos. Sci.* **36**, 838–851 (1979).
19. A. J. Heymsfield, "Ice particles observed in a cirriform cloud at -83°C and implications for polar stratospheric clouds," *J. Atmos. Sci.* **43**, 851–855 (1986).
20. K. Sassen, C. J. Grund, J. Spinhirne, M. Hardesty, and J. M. Alvarez, "The 27–28 October 1986 FIRE IFO cirrus case study: a five lidar overview of cloud structure and evolution," *Mon. Weather Rev.* **118**, 2288–2311 (1990).



Plate 1. Pastel primary rainbow photographed near Marion Center, PA.



Plate 2. Portion of a primary rainbow photographed in State College, PA.



Plate 3. Vivid primary rainbow photographed in Seattle, WA. Photograph courtesy of A. B. Fraser.



Plate 4. The \perp -polarized component of a rainbow seen in Seattle, WA. Photograph courtesy of A. B. Fraser.



Plate 5. The \perp -polarized component of a rainbow seen in Boulder, CO. Photograph courtesy of A. B. Fraser.

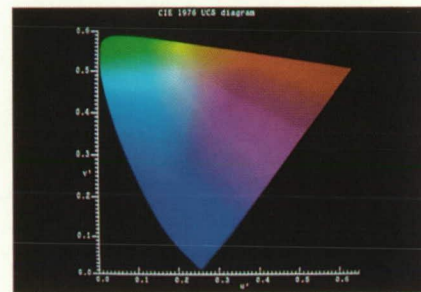


Plate 6. The CIE 1976 UCS diagram as photographed from a computer's red-green-blue color monitor.



Plate 7. The \parallel -polarized counterpart of Fig. 5. Photograph courtesy of A. B. Fraser.



Plate 8. Corona with three red rings photographed by one of the authors (J. A. Lock) on 22 Aug. 1989. The photo also shows some iridescence near the edges of the cloud far from the location of the corona.



Plate 9. Fogbow on Mauna Kea Summit (13,760 ft).



Plate 10. Fogbow on Mauna Kea flank (10,500 ft).



Plate 11. Fogbow in marine stratus.



(a)



(b)



(c)



(d)

Plate 12. Color photographs of solar corona displays from cirrus ice crystal clouds obtained at (a) 2229 on 6 Apr. 1989, (b) 2306 on 6 Apr. 1990, and (c) 2100 and (d) 2233 on 3 June 1990. All the photographs were taken with a 55-mm lens using a polarizing filter.

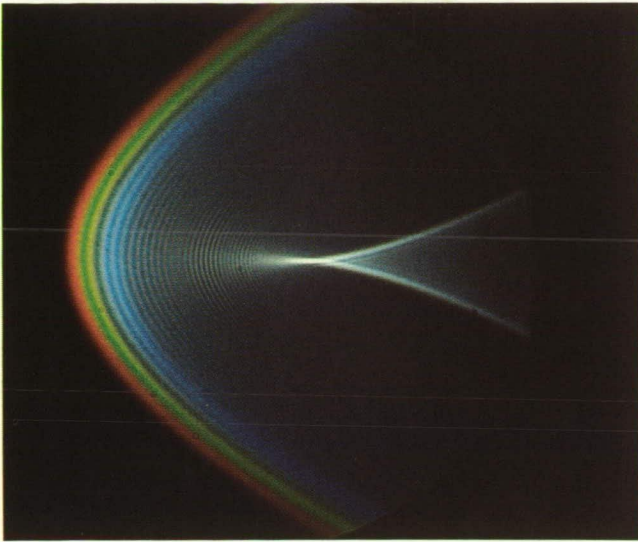


Plate 13. Photograph of the rainbow region of an oblate water drop illuminated by white light from a xenon lamp. The arc on the left is associated with the usual Airy caustic while near the center is a transverse cusp caustic. The horizontal scattering angle θ increases from left to right where $\theta \approx 152^\circ$ on the right edge of the pattern recorded. Diameter D of the drop was 1.9 mm.

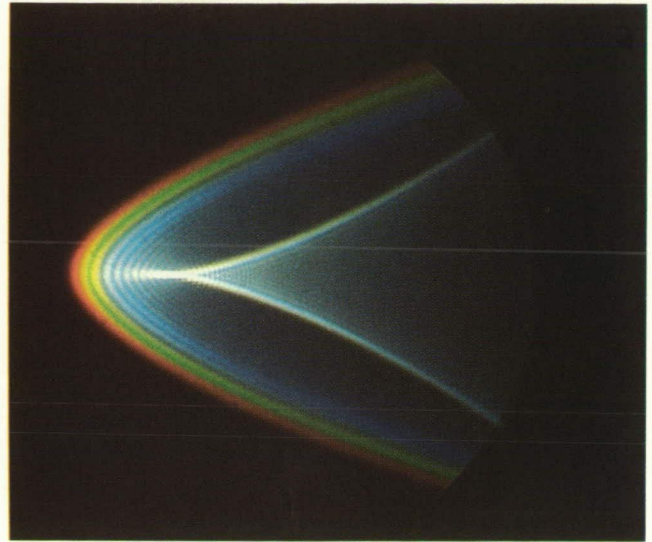


Plate 14. Photograph of scattering from a drop as in Plate 13 but with the oblateness increased so that the Airy caustic and cusp are closer. Diameter D of the drop was 1.8 mm.

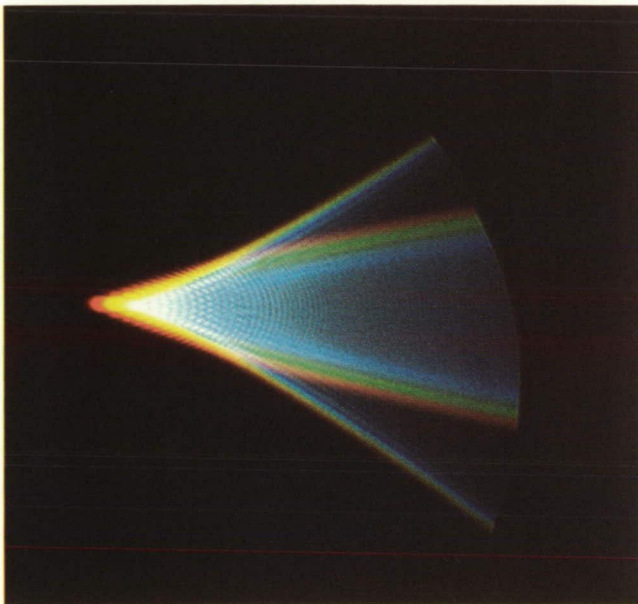


Plate 15. Photograph of scattering from a drop for a shape at or close to that giving a HUFFS. The cusp and Airy caustics have merged. Diameter D of the drop was 2.1 mm and the scattering was vertically polarized.

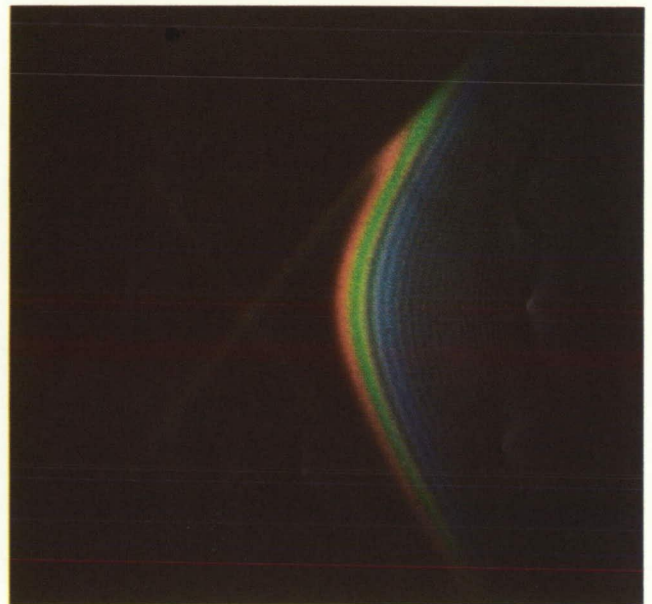


Plate 16. Photograph of an unidentified caustic produced in the rainbow region of a highly oblate drop of water. The horizontal scattering angle θ increases from left to right. The colored arc on the right crosses the midplane near the angular location of the usual Airy caustic for the primary rainbow. The lack of symmetry about the midplane for this particular photograph may be a consequence of either imperfect symmetry of the drop or imperfect alignment of the incident beam with the equatorial plane of the drop.



Plate 17. The multicolored pattern in this photograph taken through a polarizing filter results from transformations of partially polarized skylight on transmission by the stress-induced birefringent airplane window. Not all colors are seen with equal probability or have equal maximum purity. Pure oranges and reds are conspicuous by their absence. The purest colors are purples and yellowish-greens.



Plate 18. Skylight is neither uniform in color nor in brightness, varying from bright white near the horizon to dark blue overhead.



Plate 19. This polarizing filter enclosed within a birefringent plastic case was photographed under tungsten illumination with a polarizing filter on the camera. The colors are purer and span a wider gamut than those shown in Plate 17 because tungsten light is redder than skylight and the degree of polarization of the light incident on the case is higher than that of skylight.



Plate 20. Photograph of colored bands associated with the transition to total reflection from bubbles in a cloud. The most pronounced band is a red-yellow band located just above an imaginary horizontal line drawn half-way up the picture. A second fainter band is present above it near the left side. Reflections from the window are visible near the right side. The focal length of the camera lens was 50 mm.



Plate 21. Successive mountain ridges #1.



Plate 22. Successive mountain ridges #2.

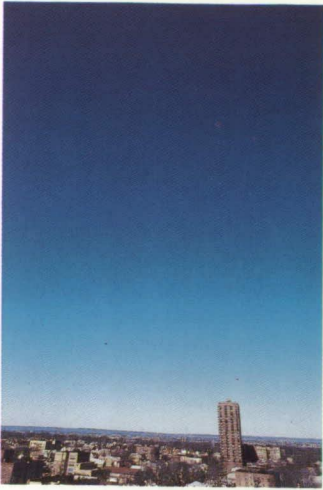


Plate 23. Gradation of sky color from the horizon up over Cliffside Park, N.J.



Plate 26. Transparency. Wilson Hurley, *Towering Cumulus*. Oil on Canvas, 1977.



Plate 29. Brightness difference between cumulus and cirrocumulus, Haines Falls, N.Y. Cumulus is illuminated by reflected sunlight, optically thinner cirrocumulus by transmitted sunlight.

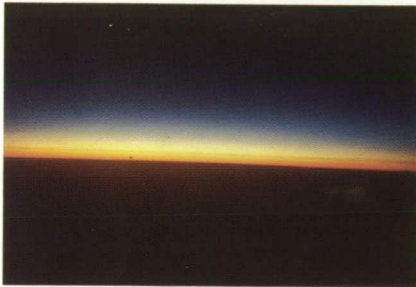


Plate 24. Gradation of sky color from horizon up after sunset over Egypt.



Plate 27. Color gradation just before sunset in two small cumulonimbus over New York City.



Plate 30. Dark fractostratus beneath an altostratus deck over Cliffside Park, NJ. Compare with Plate 31.



Plate 25. Twilight scene after sunset near White Plains, N.Y., resembling Frederic Church's *Twilight in the Wilderness*.



Plate 28. Color difference between strato-cumulus and cirrus near sunset at San Diego, CA.



Plate 31. Lighter fractostratus beneath a dark stratus deck over Cliffside Park, NJ. Compare with Plate 30.

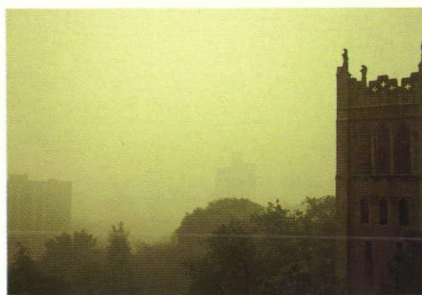


Plate 32. Sky with strange orange hue during intense shower (no thunder) looking south over New York City.



Plate 33. Crepuscular rays passing through a break in a stratocumulus deck late afternoon over Cliffside Park, NJ. Some rays are broad, while others are pencil thin.



Plate 34. Rainbow over Niagara Falls but beneath nonprecipitating stratocumulus of late afternoon, showing the shadow of late afternoon crossing the bow at 90° .



Plate 35. Pair of seated, crowned, and flute-playing figures beneath red-white-red (~ 10 -cm) rainbow pictographs, below a large bird figure from Ceremonial Cave, Canyon de Chelly, Ariz.



Plate 36. Classic Fremont rock art panel, both pecked and painted, located high above Feron Creek in the western San Rafael Swell region of Utah. The main ~ 2 -m-diameter rainbow shelters a triad of large ceremonial figures, along with numerous concentric circles and other figures. To the right of this panel are a red-white-red rainbow and a single-arc rainbow that spreads from the outstretched hands of a horned Fremont anthropomorph.



Plate 37. Multicolored (~40-cm) rainbow from a small shelter in Red Hole Wash in the western San Rafael Swell region of Utah, also containing red Fremont anthropomorphs. This figure depicts the proper colorization for the primary rainbow and also encloses concentric circles that could represent the approximate antisolar point.



Plate 38. Pictograph of a decorated Jornada froglike creature from a small rock shelter near Chloride, N.M. The rainbow arc that spreads from the fingertips of this zoomorph is ~25 cm in diameter.



Plate 39. Hissink's elliptical halo in Kuopio, Finland, on 18 Feb. 1988 at 10:36 GMT. The vertical diameter of this phenomenon is ~10–11°. Photograph by Juhana Hakumäki.



Plate 40. Schlesinger's elliptical halo (vertical diameter ~7°) in Kuopio, Finland, on 13 May 1989. Photograph by Juhana Hakumäki at 10:13 GMT with a 28-mm lens. Hissink's and Schlesinger's elliptical halos are as of yet theoretically unexplained phenomena to the best of our knowledge.